

# Topological transformation of synthetic ferromagnetic skyrmions: thermal assisted switching of helicity by spin-orbit torque

Received: 9 January 2024

Accepted: 25 November 2024

Published online: 02 December 2024

Check for updates

Kai Wu<sup>1,9</sup>, Yuelei Zhao<sup>1,9</sup>, Hongyuan Hao<sup>2,9</sup>, Sheng Yang<sup>1</sup>, Shuang Li<sup>1</sup>, Qingfang Liu<sup>2</sup>, Senfu Zhang<sup>2,3</sup>✉, Xixiang Zhang<sup>3</sup>, Johan Åkerman<sup>4,5,6</sup>, Li Xi<sup>2</sup>, Ying Zhang<sup>7</sup>, Kaiming Cai<sup>8</sup> & Yan Zhou<sup>1</sup>✉

This study demonstrates the controllable switching of skyrmion helicity using spin-orbit torque, enhanced by thermal effects. Electric current pulses applied to a [Pt/Co]<sub>3</sub>/Ru/[Co/Pt]<sub>3</sub> multilayer stripe drive skyrmions in a direction opposite to the current flow. Continuous pulsing results in an unexpected reversal of skyrmion motion. Micromagnetic simulations reveal that skyrmions in the upper and lower ferromagnetic layers exhibit distinct helicities, forming a hybrid synthetic skyrmion. The helicity switch of this hybrid structure accounts for the motion reversal. This study introduces innovative helicity control methods, advancing spintronic device applications, including data storage and quantum computing based on skyrmion helicity.

Topological magnetic structures, such as magnetic skyrmions<sup>1–6</sup>, skyrmionium<sup>7–10</sup>, meron<sup>11,12</sup>, bobber<sup>13,14</sup>, soliton<sup>15,16</sup>, biskyrmion<sup>17</sup>, bimeron<sup>18–20</sup> and their derivative structures<sup>21–23</sup>, have gained significant research attention due to their unique physical properties and potential applications in spintronics<sup>24</sup>. The non-collinear spin textures arise from the interplay between various energy terms. These include the Heisenberg exchange interaction, Dzyaloshinskii–Moriya interaction (DMI), dipolar interaction energy, magnetic anisotropy, and Zeeman energy. The topological spin textures can be described by three different topological degrees of freedom based on the out-of-plane and in-plane spin configuration<sup>25</sup>: the topological charge  $Q_z$ <sup>26</sup>, which represents the number of times the magnetization vector  $\mathbf{m}$  wraps the unit sphere; the vorticity number  $Q_v$ <sup>27</sup>, which represents the angle integration of the magnetic moment of the domain wall along the circumferential direction; and the helicity number  $Q_h$ <sup>28</sup>, which defines the in-plane magnetization-swirling direction. Transformations between some of the topological spin textures can be achieved by controlling the energy through the

application of magnetic field<sup>16,29</sup>, spin transfer torque<sup>4,28</sup>, spin-orbit torque<sup>7</sup>, electric field<sup>30</sup>, or thermal fluctuation<sup>20,31,32</sup>, accompanied by changes occurring in one or more of the three degrees of freedom. However, in most cases, the non-collinear spin textures are stabilized mainly by DMI, which favors a right angle between the adjacent magnetic spins, resulting in topological spin textures with a fixed rotation fashion<sup>2</sup>. In this case, some degree of freedom, in particular  $Q_h$ , is locked by the sign of the DMI. The manipulation of the helicity number has been a long-standing goal for spintronic devices in binary information processing<sup>33</sup> and quantum computation<sup>34</sup>. Two main approaches have been proposed to achieve this goal: (i) by controlling the DMI through the application of an electric field or other means<sup>30</sup>, and (ii) by choosing centrosymmetric materials that lack chiral DMI, such as frustrated magnet Fe<sub>3</sub>Sn<sub>2</sub> and Ba(Fe<sub>1-x</sub>-<sub>0.05</sub>Sc<sub>x</sub>Mg<sub>0.05</sub>)<sub>12</sub>O<sub>19</sub> ( $x = 0.16$ )<sup>26,28,35</sup>. However, in the (i) case, it is difficult to achieve a large range of DMI control<sup>30</sup>, and in the (ii) case, the two states with opposite helicities degenerate, resulting in random switching rather than controlled switching<sup>28</sup>.

<sup>1</sup>School of Science and Engineering, The Chinese University of Hong Kong, Shenzhen, Shenzhen, China. <sup>2</sup>School of Physical Science and Technology, Lanzhou University, Lanzhou, China. <sup>3</sup>Physical Science and Engineering Division, King Abdullah University of Science and Technology, Thuwal, Saudi Arabia. <sup>4</sup>Department of Physics, University of Gothenburg, Gothenburg, Sweden. <sup>5</sup>Center for Science and Innovation in Spintronics, Tohoku University, 2-1-1 Katahira, Aoba-ku, Sendai, Japan. <sup>6</sup>Research Institute of Electrical Communication, Tohoku University, 2-1-1 Katahira, Aoba-ku, Sendai, Japan. <sup>7</sup>State Key Laboratory of Magnetism, Beijing National Laboratory for Condensed Matter Physics, Institute of Physics, Chinese Academy of Sciences, Beijing, China. <sup>8</sup>School of Physics, Huazhong University of Science and Technology, Wuhan, China. <sup>9</sup>These authors contributed equally: Kai Wu, Yuelei Zhao, Hongyuan Hao.

✉ e-mail: [zhangsenfu@lzu.edu.cn](mailto:zhangsenfu@lzu.edu.cn); [zhouyan@cuhk.edu.cn](mailto:zhouyan@cuhk.edu.cn)

In this study, we fabricate a  $[\text{Pt}/\text{Co}]_3/\text{Ru}/[\text{Co}/\text{Pt}]_3$  multilayer where the integration of the Ru layer creates a ferromagnetic coupling between the top and bottom ferromagnetic layers due to the Ruderman–Kittel–Kasuya–Yosida (RKKY) interaction. The interplay between DMI, RKKY interaction, dipolar interaction, and other energy factors lead us to a significant finding: skyrmions in the upper and lower ferromagnetic layers of our stacks demonstrate different helicities, leading to the formation of a unique hybrid synthetic ferromagnetic (SF) skyrmion. These hybrid SF skyrmions are generated in the film by the application of current pulses. Furthermore, we achieve controlled switching of the SF skyrmions' helicity using spin-orbit torque, aided by thermal effects, which results in their motion reversing direction after helicity switching. Micromagnetic simulations provide insights into the physical mechanisms driving these phenomena.

## Results and discussion

A multilayer stack composed of  $\text{Ta}(3)/[\text{Pt}(0.5)/\text{Co}(0.5)]_3/\text{Ru}(1.8)/[\text{Co}(0.5)/\text{Pt}(0.5)]_3/\text{TaO}_x$  with thicknesses in nanometers, depicted in Fig. 1a, is fabricated using a magnetron sputtering system. The insertion of the Ru layer between the two ferromagnetic layers is intended to introduce the ferromagnetic RKKY interaction<sup>36</sup>. The square hysteresis loop, illustrated in Fig. 1b and acquired by scanning the out-of-plane magnetic field using the MOKE microscope, displays a coercive field of  $-15$  mT. This indicates that the sample exhibits perpendicular magnetic anisotropy (PMA), and the coupling between the two PMA layers is ferromagnetic, with a positive RKKY. More information about the interlayer exchange coupling interaction can be found in our previous work<sup>36</sup>. Prior research has also confirmed the weak DMI field in this sample<sup>37</sup>.

In ferromagnetic multilayers with interfacial DMI, the DMI tends to favor the alignment of skyrmions in different layers with identical Néel orientations. Additionally, the ferromagnetic RKKY interaction between magnetic layers typically promotes parallel alignment of the magnetic moments. However, the dipole-dipole interaction favors a Bloch configuration of internal magnetization along the domain wall, as it minimizes demagnetization energy. As a result, skyrmions often undergo a thickness-dependent reorientation of their domain wall chirality, a phenomenon observed in numerous studies.<sup>38–40</sup> Similarly, in our material system, skyrmion profiles in the top and bottom layers may differ, leading to distinct helicities. Furthermore, we can control and modulate the spin texture of skyrmions in the upper and lower

layers by tuning the strength of DMI, the RKKY interaction, or other contributing energy factors. Notably, the RKKY interaction, which depends on the thickness of the Ru layer, can be varied significantly<sup>36</sup>. This tunability gives rise to a range of intriguing phenomena. For instance, as shown in Fig. 1c, we observe that the helicity of skyrmions in this material can be reversed by applying an electric current pulse.

To demonstrate the helicity reversal of skyrmions in the multilayer film, our initial step involves generating skyrmion bubbles within a  $20\text{-}\mu\text{m}$ -wide strip device, as depicted in Fig. 1c, using electrical current. Precise control over skyrmion creation and manipulation via electrical stimuli is crucial for practical applications. This method aligns well with its compatibility with complementary metal oxide semiconductor technology and its potential integration onto a chip<sup>24</sup>. Hence, our approach primarily involves employing electrical means for skyrmion creation. The process begins by saturating the device with an external magnetic field of  $+60$  mT and then gradually reducing it to  $+1$  mT. By injecting a half-sinusoidal-wave current pulse with an amplitude of  $50$  mA (equivalent to a current density of  $2.10 \times 10^{11}$  A/m<sup>2</sup>) and duration of  $500$   $\mu\text{s}$  along the  $-x$  axis of the device, numerous skyrmion bubbles are created at random positions by switching the magnetization from  $+z$  to  $-z$  direction. To minimize the interaction between different skyrmions during their motion, the density of the skyrmions should be reduced. We then increase the perpendicular field from  $+1$  mT to  $+2$  mT, and apply a sinusoidal-wave current pulse along the  $+x$  axis with an amplitude of  $42$  mA ( $1.76 \times 10^{11}$  A/m<sup>2</sup>). This helps reducing the overall skyrmion density.

We then investigate the behavior of the skyrmion bubbles driven by electric current. To move the skyrmion bubbles, we apply successive square-wave current pulses with an amplitude of  $51.7$  mA ( $2.20 \times 10^{11}$  A/m<sup>2</sup>) and a duration of  $20$   $\mu\text{s}$  along the  $+x$  axis under an out-of-plane magnetic field of  $1.4$  mT. In order to minimize the impact of Joule heating caused by the driving current, the interval between adjacent current pulses (defined as  $S$ ) is set to  $980$   $\mu\text{s}$ . For more details on the waveform of the current pulses, please refer to Fig. S1. Figure 2a shows snapshots of the skyrmion motion captured during the application of successive current pulses. It can be observed that the diameter of the skyrmion is around  $1$   $\mu\text{m}$  and it remains mostly circular shape over the whole process. The skyrmion trajectory shown in Fig. 2c reveals that the skyrmion moved in both  $x$  and  $y$  directions simultaneously. Firstly, it moves along the  $-x$  direction, opposite to the direction of the current. Secondly, it exhibits transverse motion along the  $-y$  direction, indicating the presence of the skyrmion Hall effect as expected. The skyrmion Hall angle in this experiment is approximately  $-140$  degrees in Fig. 2c.

To manipulate the skyrmions with electric current, the same amplitude and width of the current pulses used in Fig. 2a are applied. However, the interval ( $S$ ) between successive current pulses is shortened from  $980$   $\mu\text{s}$  to  $180$   $\mu\text{s}$  in order to induce more cumulative Joule heating. Due to the limited size of the device, this interval ( $180$   $\mu\text{s}$ ) is chosen to prevent the skyrmions from reaching the edge of the device along the  $y$ -axis. Figure 2b presents snapshots of the positions of a skyrmion in motion following the application of consecutive current pulses along the  $+x$  axis. The extracted trajectory of the skyrmion is shown in Fig. 2d. The diameter of the skyrmion in Fig. 2b, remains approximately  $1$   $\mu\text{m}$  as seen in Fig. 2a, is that the skyrmion moves along the current direction (i.e., the  $+x$  direction) rather than along the  $-x$  direction, as observed in Fig. 2a and c. However, it still moves along the  $-y$  direction. Figure 2b and d clearly show that as more Joule heating is introduced by shortening the interval ( $S$ ), the longitudinal direction of motion is reversed. It is also noteworthy that the skyrmion Hall angle changes from about  $-140^\circ$  to about  $-30^\circ$ . This reversal in the motion direction of the skyrmion, along with the change in the magnitude of the skyrmion Hall angle, strongly suggests a transformation in the spin structure of the skyrmion, particularly in its helicity, as the Joule heating increases.

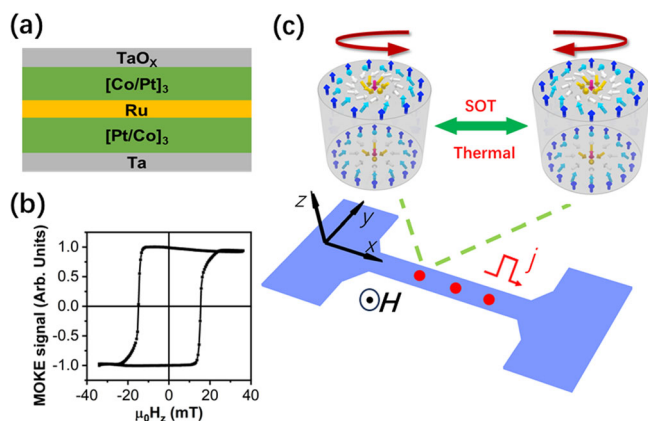


**Fig. 1 | Schematic, hysteresis loop, and device structure of multilayer SF skyrmions.** **a** Schematic diagram of the  $\text{Ta}(3)/[\text{Pt}(0.5)/\text{Co}(0.5)]_3/\text{Ru}(1.8)/[\text{Co}(0.5)/\text{Pt}(0.5)]_3/\text{Ta}(3)$  multilayers. The number in parentheses is the thickness of each layer in nanometers. **b** Hysteresis loop of the sample measured by MOKE microscope with out-of-plane field. **c** Schematic of the device and the SF skyrmions. The red arrows indicate the chirality of the skyrmion in the top FM layer.

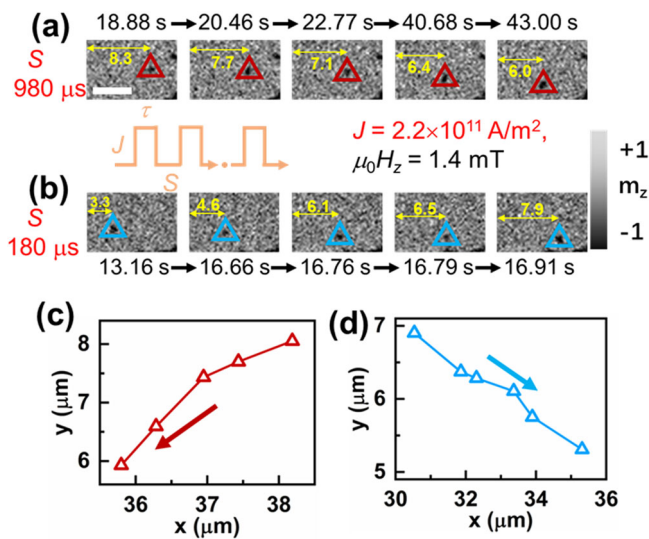


**Fig. 2 | Current-induced skyrmion bubble motion.** **a, b** The current-induced motion of skyrmion bubbles captured by MOKE microscope images reveals the distinct helicity numbers. The direction of the current is along the  $+x$  axis, and  $-1 \times 10^5$  repeating current pulses have been injected in total. The pulse is set with a duration of  $20 \mu\text{s}$  and amplitude of  $51.7 \text{ mA}$  ( $2.20 \times 10^{11} \text{ A/m}^2$ ). **a** The pulse interval is  $980 \mu\text{s}$ , while in **(b)**, the pulse interval is  $180 \mu\text{s}$ , corresponding to less Joule heating. Within the MOKE microscope images, the skyrmion bubble is depicted in red and blue triangles for **(a, b)**, respectively. The scale bar is in  $5 \mu\text{m}$ . **c, d** show the trajectories of the skyrmion bubbles, with colored triangles indicating their center positions throughout the pulse series from **(a, b)**.

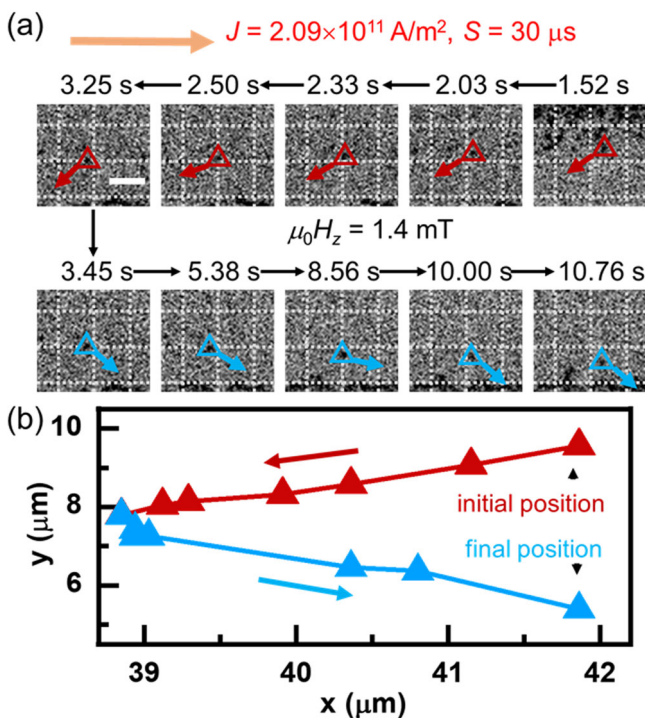


**Fig. 3 | Zigzag-type skyrmion trajectory.** **a** The MOKE microscope images depict how skyrmion bubbles with opposite helicity numbers respond when injecting the current pulses along the  $+x$  axis. **b** Zigzag-type trajectories of the skyrmion bubbles, with colored triangles indicating their center positions throughout the pulse series from **(a)**. The skyrmion bubbles are represented by red and blue triangles within the images. The pulse is set with a duration of  $20 \mu\text{s}$  and amplitude of  $49.4 \text{ mA}$  ( $2.09 \times 10^{11} \text{ A/m}^2$ ). The pulse interval was set to  $30 \mu\text{s}$  to achieve the zigzag-type trajectory. The scale bar is in  $5 \mu\text{m}$ .

Under different intervals between current pulses, we observe that the skyrmion moves in opposite longitudinal directions. However, the skyrmion under MOKE spatial resolution always moves in a fixed direction from the beginning as observed in Fig. 2. To demonstrate that the opposite directions of motion in these two cases result from changes in the magnetic structure induced by the driving current, rather than differences in the initial skyrmion spin structure, we carefully adjusted the interval and current magnitude while keeping the pulse width constant. We then observed the motion of the skyrmion at a higher time resolution. Figure 3a shows snapshots of the moving skyrmion when the interval and current density are reduced to  $30 \mu\text{s}$  and  $2.09 \times 10^{11} \text{ A/m}^2$ , respectively, with the current direction along the  $+x$  axis. Although the skyrmion encounters some pinning sites that temporarily trap it, it eventually escapes and resumes its motion. However, the trajectory of the skyrmion bubbles deviates from a straight path. Instead, they initially move toward the lower left corner for a certain distance before abruptly shifting direction toward the lower right corner, as illustrated in Fig. 3b. Furthermore, when the current direction reverses along the  $-x$  axis (as shown in Fig. S2c, d), the motion of the skyrmion bubble also reverses. This means that after advancing a certain distance towards the upper right corner, the skyrmion suddenly changes direction, moving towards the upper left corner. These observations suggest that both the applied current and Joule heating contribute to the reversal of the skyrmion's motion. It is highly likely that the spin texture of the skyrmion undergoes changes during its movement.

To elucidate the unexpected reversal in the motion direction of skyrmions observed in our experiment, we employ micromagnetic simulations to investigate the underlying physical mechanism. Our research centers on a bilayer structure composed of two magnetically coupled layers via the RKKY interaction (detailed simulation methods are described in the methods section). Our analysis reveals that the spin texture of skyrmions within the bilayer film is predominantly governed by the combined effects of DMI, dipole interaction, and RKKY interaction (Fig. S3). Figure 4a shows the relationship between the skyrmion helicity of the top and bottom layers and the strength of DMI. The results indicate that the helicity of the bottom layer remains relatively constant, while the helicity of the top layer decreases from  $\pi$  to 0 as DMI increases from 0 to  $1.5 \text{ mJ/m}^2$ . When DMI is greater than  $1.3 \text{ mJ/m}^2$ , it dominates the spin structure of the skyrmion, resulting in both the top and bottom layers being Néel-type skyrmions with a helicity of 0. As DMI decreases, the dipole interaction becomes more significant, causing the magnetic moments in the two layers to become anti-parallel gradually to achieve magnetic circuit closure. This results in the helicity of the skyrmions in the top layer gradually increasing from 0 to  $\pi$ . When DMI is less than  $0.3 \text{ mJ/m}^2$ , the magnetic moments in the top and bottom layers become almost antiparallel. Interestingly, after applying an electric current to the bilayer film, the helicity of skyrmions can be flipped by spin-orbit torque for a wide range of helicity values. Figure 4b illustrates the relationship between critical DMI and driving current. For example, when the driving current is  $3.6 \times 10^{11} \text{ A/m}^2$ , if DMI is greater than  $0.78 \text{ mJ/m}^2$ , the skyrmion will maintain its previous helicity, but if DMI is less than  $0.78 \text{ mJ/m}^2$ , the helicity of the skyrmion will flip. Figure 4c illustrates the total energy of the system and the topological number of the skyrmion over simulation time for  $D = 0.77$  and  $0.78 \text{ mJ/m}^2$ , respectively. The comparison between the two cases indicates that, for  $D = 0.77 \text{ mJ/m}^2$ , the skyrmion has crossed a potential barrier during the helicity flip, unlike the case of  $D = 0.78 \text{ mJ/m}^2$ . Notably, the energies of the skyrmion at zero current before and after the helicity flip are identical, indicating that the skyrmion with opposite helicity signs is equally stable. Additionally, the topological number remains constant at approximately  $-1$  during the helicity flipping process, suggesting that the flipping process is completed without breaking the topological charge of the skyrmion. To observe the process of skyrmion helicity flipping and the resulting



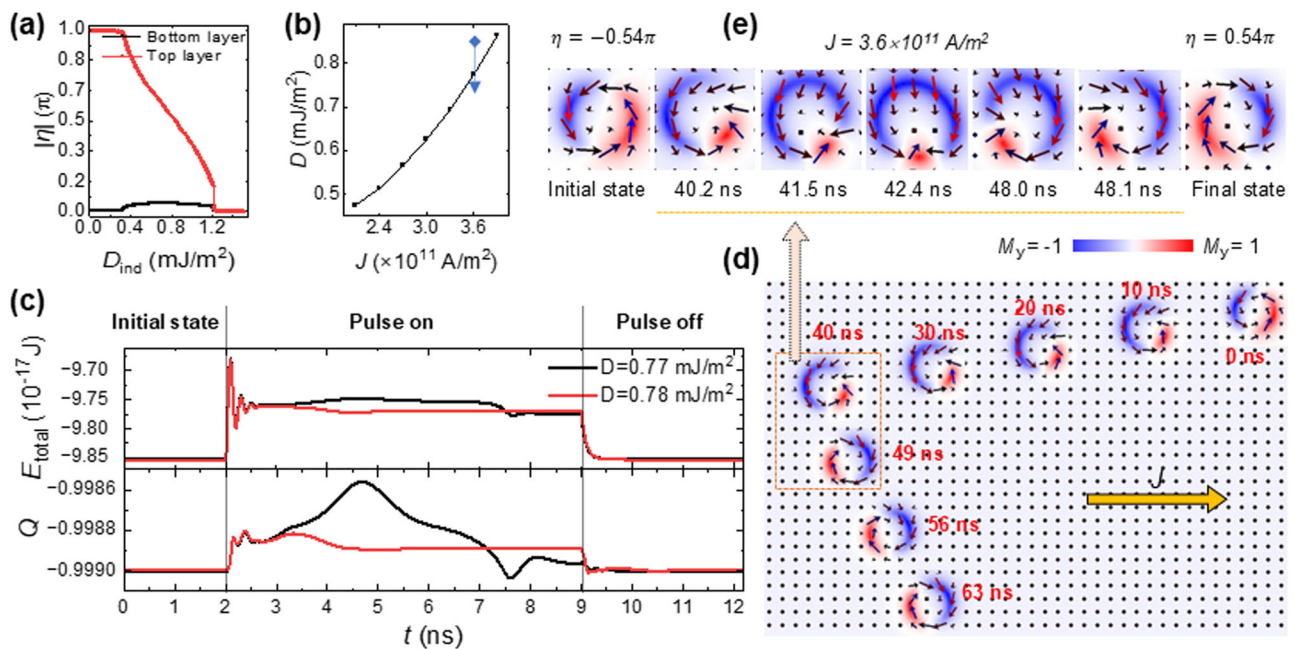


**Fig. 4 | Simulation results of skyrmion helicity reversal.** **a** The relationship between the skyrmion helicity of the top and bottom layers and the strength of DMI. **b** The critical DMI as a function of driving current density. **c** Total energy of the system and the topological number of the skyrmion over simulation time for  $D = 0.77$  and  $0.78$  mJ/m<sup>2</sup>, respectively. **d** Trajectory of the skyrmion and the

corresponding spin structure when a current density of  $3.6 \times 10^{11}$  A/m<sup>2</sup> is applied for a duration of 63 ns. The DMI was initially 0.78 mJ/m<sup>2</sup> for the first 40 ns and then decreased to 0.77 mJ/m<sup>2</sup> for the remaining 23 ns. **e** Evolution of the spin texture during the helicity flipping process. The skyrmion helicity flip to  $+0.54\pi$  from  $-0.54\pi$ .

changes in its motion, we conducted calculations on the trajectory of skyrmion movement and the variation of spin structure. The simulation was done under a current density of  $3.6 \times 10^{11}$  A/m<sup>2</sup> for a duration of 63 ns. The DMI was initially 0.78 mJ/m<sup>2</sup> for the first 40 ns and then decreased to 0.77 mJ/m<sup>2</sup> for the remaining 23 ns. The results, as shown in Fig. 4d, indicate that prior to the application of the current pulse, the skyrmion helicity was approximately  $-0.54\pi$ . After the current was applied, the spin structure at the boundary of the skyrmion slightly deformed and the skyrmion moved towards the lower left corner. At 40 ns, the DMI decreased to 0.77 mJ/m<sup>2</sup>. As a result, the helicity of the skyrmion flipped by the spin-orbit torque (SOT), causing the trajectory of the skyrmion to change towards the lower right. This observation aligns with our experimental findings. Figure 4e provides detailed images of the helicity flipping process after 40 ns. It can be observed that under the influence of the SOT<sup>41–43</sup>, the blue region ( $M_y < 0$ ) at the boundary of the skyrmion rapidly expands from the top, while the red region ( $M_y > 0$ ) shrinks rapidly. The red region continues to shrink and maintains its position just at the bottom before gradually moving to the lower left corner, then rapidly expanding to the left and achieving the helicity flipping with the skyrmion helicity changing to  $+0.54\pi$ .

It is clearly observed that the micromagnetic simulation results shown in Fig. 4d reveal a difference in the absolute value of the intrinsic skyrmion Hall angle before and after helicity reversal. This discrepancy arises because our simulations consider an idealized, defect-free sample, whereas the real sample contains significant disorder and the skyrmion motion falls within the creep motion regime. According to previous reports<sup>44,45</sup>, skyrmion motion in the creep regime does not accurately reflect the intrinsic Hall angle. Additionally, deformations in the spin texture can alter the Hall angle. As a result, the Hall angle observed in our experiments is difficult to be investigated quantitatively.

Measurements were conducted at different temperatures using a heating stage, and the results are shown in Fig. S4. It demonstrates that an increase in temperature of just around 12 °C is sufficient to reverse the direction of skyrmion motion. Besides, Lorentz transmission

electron microscopy measurements are performed, as shown in Fig. S5. However, the Bloch-type component is not distinguishable. More details can be found in supplement materials. Both the temperature-dependent experiments and micromagnetic simulation results indicate that the key reason for the reversal of skyrmion motion direction is the inversion of skyrmion helicity induced by the SOT. Once the current reaches a critical value, SOT can flip the skyrmion helicity. However, in our experiment with the multilayer thin film, controlling the magnitude of the driving current presents significant challenges due to the material's disorder. Insufficient current density fails to initiate skyrmion motion, whereas excessive current density can either create multiple new skyrmions or obliterate the existing ones. This situation limits the feasible range of current density, rendering skyrmion helicity flipping through increased current density impractical. However, our micromagnetic simulation analysis suggests an alternative approach: adjusting the material's magnetic parameters, such as reducing the strength of DMI, can lower the critical current density required to flip skyrmion helicity. Initially, at room temperature, the skyrmions moved opposite to the direction of the current. However, as the current was applied over time, the temperature of the sample increased, leading to a decrease in DMI strength. Once the DMI reached a critical threshold, the current induced a flip in the helicity of the skyrmion, reversing its motion direction. Please note that the parameters used in the simulations may differ from those of the actual samples, but the physical mechanisms remain similar.

In this study, we fabricate multilayer stacks composed of [Pt/Co]<sub>3</sub>/Ru/[Co/Pt]<sub>3</sub> layers. The integration of the Ru layer creates a ferromagnetic RKKY interaction between the top and bottom ferromagnetic layers. Our combined experimental and micromagnetic simulation analyses reveal the presence of different helicities in the skyrmions of the upper and lower ferromagnetic layers, leading to the formation of a hybrid synthetic ferromagnetic skyrmion. We demonstrate the ability to manipulate the helicity of these SF skyrmions using spin-orbit torque, enhanced by thermal effects, which results in a sudden reversal in their velocity component parallel to the electric

current direction. Detailed micromagnetic simulations are conducted to understand the underlying physical mechanisms. This research provides a method for controlling skyrmion helicity reversal, opening possibilities for the development of advanced spintronic devices that leverage skyrmion helicity.

## Methods

### Sample preparation

The multilayer stack Ta(3)/[Pt(0.5)/Co(0.5)]<sub>3</sub>/Ru(1.8)/[Co(0.5)/Pt(0.5)]<sub>3</sub>/TaO<sub>x</sub> (thicknesses are in nanometers) is deposited onto a Si wafer with a 300-nm-thick oxide layer at room temperature, using a high-vacuum magnetron sputtering system (AJA International Inc.). The base pressure of the vacuum system is below  $4 \times 10^{-6}$  Pa. The device, with Ru thickness of approximately 1.8 nm, induces ferromagnetic coupling of the upper and lower Pt/Co magnetic layers. The bottom Ta layer acts as a spin-current source that generates SOT for skyrmion bubble motion. Using lift-off photolithography, the multilayer is patterned to a 20- $\mu$ m-wide device which is then attached to a homemade printed circuit board and bonded with electrodes for different pulse injections (Keithley 6221 current source). All the current densities are on the order of  $10^{11}$  A/m<sup>2</sup>.

### Measurement of current-driven skyrmion dynamics

To directly image the skyrmion bubbles, a MOKE microscope with a 50 $\times$  objective lens is used. In the resulting MOKE images, regions depicted in gray correspond to magnetization pointing up, while black regions correspond to magnetization pointing down. To nucleate the skyrmion bubbles shown in Figs. 2 and 3, a current pulse lasting 500  $\mu$ s is applied at a current density of  $\sim 2.10 \times 10^{11}$  A/m<sup>2</sup>. The skyrmions in Fig. 2c, d are generated by extending the skyrmion bubbles using a current-driven method in +10 mT field. The skyrmion bubbles are propelled using a train of repeating square-wave current pulses.

### Micromagnetic calculations

Micromagnetic simulations are performed by Mumax3 software. Considering that the three Pt/Co layers at the top are coupled to the three Co/Pt layers below through RKKY interaction due to the interlayer Ru. Thus, to simplify the calculation, in the simulations, we studied a bilayer structure consisting of two magnetic layers coupled by RKKY interaction. The mesh size was set to  $3 \times 3 \times 3$  nm<sup>3</sup> and the following parameters were chosen: the saturation magnetization  $M_s = 1.0 \times 10^6$  A m<sup>-1</sup>, the perpendicular anisotropy  $K_u = 6.9 \times 10^5$  J m<sup>-3</sup>, the exchange stiffness  $A = 1.5 \times 10^{-11}$  J m<sup>-1</sup>, the exchange stiffness between the two ferromagnetic layers  $A_{\text{inter}} = 0.8 \times 10^{-13}$  J m<sup>-1</sup>, and interfacial DMI constant  $D$  ranging from 0 to  $1.5 \times 10^{-3}$  J m<sup>-2</sup>.

### Data availability

The authors declare that the data supporting the findings of this study is available within the article and its Supplementary Information file. All other data that support the results of this study are available from the corresponding author upon reasonable request.

### Code availability

The source code of Mumax3 is available at <https://mumax.github.io/>.

## References

- Jiang, W. et al. Blowing magnetic skyrmion bubbles. *Science* **349**, 283–286 (2015).
- Nagaosa, N. & Tokura, Y. Topological properties and dynamics of magnetic skyrmions. *Nat. Nanotechnol.* **8**, 899–911 (2013).
- Zhou, Y. Magnetic skyrmions: intriguing physics and new spintronic device concepts. *Natl. Sci. Rev.* **6**, 210–212 (2018).
- Wang, W. et al. Electrical manipulation of skyrmions in a chiral magnet. *Nat. Commun.* **13**, 1593 (2022).
- Fert, A., Cros, V. & Sampaio, J. Skyrmions on the track. *Nat. Nanotechnol.* **8**, 152–156 (2013).
- Zhang, S. et al. Current-induced magnetic skyrmions oscillator. *New J. Phys.* **17**, 023061 (2015).
- Yang, S. et al. Reversible conversion between skyrmions and skyrmioniums. *Nat. Commun.* **14**, 3406 (2023).
- Bo, L. et al. Formation of skyrmion and skyrmionium in confined nanodisk with perpendicular magnetic anisotropy. *J. Phys. D: Appl. Phys.* **53**, 195001 (2020).
- Zhang, S., Kronast, F., van der Laan, G. & Hesjedal, T. Real-space observation of skyrmionium in a ferromagnet-magnetic topological insulator heterostructure. *Nano Lett.* **18**, 1057–1063 (2018).
- Zhang, X. et al. Control and manipulation of a magnetic skyrmionium in nanostructures. *Phys. Rev. B* **94**, 094420 (2016).
- Yu, X. Z. et al. Transformation between meron and skyrmion topological spin textures in a chiral magnet. *Nature* **564**, 95–98 (2018).
- Xia, J., Zhang, X., Liu, X., Zhou, Y. & Ezawa, M. Qubits based on merons in magnetic nanodisks. *Commun. Mater.* **3**, 88 (2022).
- Zheng, F. et al. Experimental observation of chiral magnetic bobbers in B20-type FeGe. *Nat. Nanotechnol.* **13**, 451–455 (2018).
- Ran, K. et al. Creation of a chiral bobber lattice in helimagnet-multilayer heterostructures. *Phys. Rev. Lett.* **126**, 017204 (2021).
- Caretta, L. et al. Relativistic kinematics of a magnetic soliton. *Science* **370**, 1438–1442 (2020).
- Li, L. et al. Transformation from magnetic soliton to skyrmion in a monoaxial chiral magnet. *Adv. Mater.* **35**, 2209798 (2023).
- Yu, X. Z. et al. Biskyrmion states and their current-driven motion in a layered manganite. *Nat. Commun.* **5**, 3198 (2014).
- Li, X. et al. Bimeron clusters in chiral antiferromagnets. *NPJ Comput. Mater.* **6**, 169 (2020).
- Hu, G. et al. Voltage-controlled bimeron diode-like effect in nanoscale information channel. *J. Phys. D: Appl. Phys.* **56**, 085001 (2023).
- Ohara, K. et al. Reversible transformation between isolated skyrmions and bimerons. *Nano Lett.* **22**, 8559–8566 (2022).
- Nayak, A. K. et al. Magnetic antiskyrmions above room temperature in tetragonal Heusler materials. *Nature* **548**, 561–566 (2017).
- Bera, S. & Mandal, S. S. Theory of the skyrmion, meron, anti-skyrmion, and antimeron in chiral magnets. *Phys. Rev. Res.* **1**, 033109 (2019).
- Zheng, F. et al. Skyrmion–antiskyrmion pair creation and annihilation in a cubic chiral magnet. *Nat. Phys.* **18**, 863–868 (2022).
- Yu, G. et al. Room-temperature skyrmion shift device for memory application. *Nano Lett.* **17**, 261–268 (2017).
- Zhang, X. et al. Skyrmion-electronics: writing, deleting, reading and processing magnetic skyrmions toward spintronic applications. *J. Phys.: Condens. Matter.* **32**, 143001 (2020).
- Wei, W. et al. Current-controlled topological magnetic transformations in a nanostructured kagome magnet. *Adv. Mater.* **33**, 2101610 (2021).
- Zou, J., Kim, S. K. & Tserkovnyak, Y. Topological transport of vorticity in Heisenberg magnets. *Phys. Rev. B* **99**, 180402 (2019).
- Hou, Z. et al. Current-induced helicity reversal of a single skyrmionic bubble chain in a nanostructured frustrated magnet. *Adv. Mater.* **32**, 1904815 (2020).
- Lv, X. et al. Controllable topological magnetic transformations in the thickness-tunable van der Waals ferromagnet Fe<sub>5</sub>GeTe<sub>2</sub>. *ACS Nano* **16**, 19319–19327 (2022).
- Dai, B. et al. Electric field manipulation of spin chirality and skyrmion dynamic. *Sci. Adv.* **9**, 6836 (2023).
- Yu, X. Z. et al. Thermally activated helicity reversals of skyrmions. *Phys. Rev. B* **93**, 134417 (2016).
- Nakatani, Y., Yamada, K. & Hirohata, A. Switching of skyrmion chirality by local heating. *Sci. Rep.* **9**, 13475 (2019).

33. Wei, W. et al. Current-controlled topological magnetic transformations in a nanostructured kagome magnet. *Adv. Mater.* **33**, 2170260 (2021).
34. Xia, J., Zhang, X., Liu, X., Zhou, Y. & Ezawa, M. Universal quantum computation based on nanoscale skyrmion helicity qubits in frustrated magnets. *Phys. Rev. Lett.* **130**, 106701 (2023).
35. Yu, X. et al. Magnetic stripes and skyrmions with helicity reversals. *Proc. Natl. Acad. Sci. USA* **109**, 8856–8860 (2012).
36. Zhao, Y. et al. Domain wall dynamics in ferromagnet/Ru/ferromagnet stacks with a wedged spacer. *Appl. Phys. Lett.* **119**, 022406 (2021).
37. Wu, K. et al. Tunable skyrmion–edge interaction in magnetic multilayers by interlayer exchange coupling. *AIP Adv.* **12**, 055210 (2022).
38. Zhang, S., Zhang, J., Wen, Y., Chudnovsky, E. M. & Zhang, X. Determination of chirality and density control of Néel-type skyrmions with in-plane magnetic field. *Commun. Phys.* **1**, 36 (2018).
39. Soumyanarayanan, A. et al. Tunable room-temperature magnetic skyrmions in Ir/Fe/Co/Pt multilayers. *Nat. Mater.* **16**, 898–904 (2017).
40. Meijer, M. J. et al. Magnetic chirality controlled by the interlayer exchange interaction. *Phys. Rev. Lett.* **124**, 207203 (2020).
41. He, W. et al. Field-free spin–orbit torque switching enabled by the interlayer Dzyaloshinskii–Moriya interaction. *Nano Lett.* **22**, 6857–6865 (2022).
42. Kolesnikov, A. G., Stebliy, M. E., Samardak, A. S. & Ognev, A. V. Skyrmionium—high velocity without the skyrmion Hall effect. *Sci. Rep.* **8**, 16966 (2018).
43. Stebliy, M. E. et al. Experimental evidence of skyrmion-like configurations in bilayer nanodisks with perpendicular magnetic anisotropy. *J. Appl. Phys.* **117**, 17B529 (2015).
44. Litzius, K. et al. Skyrmion Hall effect revealed by direct time-resolved X-ray microscopy. *Nat. Phys.* **13**, 170–175 (2017).
45. Jiang, W. et al. Direct observation of the skyrmion Hall effect. *Nat. Phys.* **13**, 162–169 (2017).

## Acknowledgements

Y.Z. acknowledges funding support by Shenzhen Fundamental Research Fund (Grant No. JCYJ20210324120213037), the National Natural Science Foundation of China (Grant No. 12374123 and 12204396), Guangdong Basic and Applied Basic Research Foundation (2021B1515120047), Shenzhen Peacock Group Plan (KQTD20180413181702403) and the 2023 SZSTI stable support scheme. Y.L.Z. acknowledges funding support from the National Natural Science Foundation of China (Grant No. 12004319). S.F.Z. acknowledges funding support from the National Natural Science Foundation of China (Grant No. 12104197 and 12474115). X.X.Z. acknowledges funding support by King Abdullah University of Science and Technology (KAUST), Office of Sponsored Research (OSR) under Award Nos. ORA-CRG8-2019-4081 and ORA-CRG10-2021-4665. L.X. acknowledges funding support from

the National Natural Science Foundation of China (Grant No. 51671098). Y.Z. acknowledges funding support from the National Natural Science Foundation of China (Grant No. 52271195).

## Author contributions

Y.Z. (Yan Zhou) conceived the work and supervised the project. K.W., Y.L.Z., H.H.Y., and S.Y. performed the experiments under the supervision of Y.Z. (Yan Zhou). S.L., H.H.Y., and S.F.Z. carried out the simulation under the supervision of S.F.Z. All authors participated in discussions regarding the results and contributed to the preparation of the manuscript.

## Competing interests

The authors declare no competing interests.

## Additional information

**Supplementary information** The online version contains supplementary material available at <https://doi.org/10.1038/s41467-024-54851-5>.

**Correspondence** and requests for materials should be addressed to Senfu Zhang or Yan Zhou.

**Peer review information** *Nature Communications* thanks Alexander Samardak and the other anonymous reviewer(s) for their contribution to the peer review of this work. A peer review file is available.

**Reprints and permissions information** is available at <http://www.nature.com/reprints>

**Publisher's note** Springer Nature remains neutral with regard to jurisdictional claims in published maps and institutional affiliations.

**Open Access** This article is licensed under a Creative Commons Attribution-NonCommercial-NoDerivatives 4.0 International License, which permits any non-commercial use, sharing, distribution and reproduction in any medium or format, as long as you give appropriate credit to the original author(s) and the source, provide a link to the Creative Commons licence, and indicate if you modified the licensed material. You do not have permission under this licence to share adapted material derived from this article or parts of it. The images or other third party material in this article are included in the article's Creative Commons licence, unless indicated otherwise in a credit line to the material. If material is not included in the article's Creative Commons licence and your intended use is not permitted by statutory regulation or exceeds the permitted use, you will need to obtain permission directly from the copyright holder. To view a copy of this licence, visit <http://creativecommons.org/licenses/by-nc-nd/4.0/>.

© The Author(s) 2024